Size effects in cellular solids

Tekoğlu, Cihan

2 Discrete Analysis of Size Effects

In this chapter, we analyze size effects in the mechanical behaviour of cellular solids. For this purpose, we perform simple shear, uniaxial compression and pure bending tests on two-dimensional cellular materials, having regular (squares, hexagons) and irregular (perturbed hexagons, Voronoi tessellations) microstructures. We change the size of the samples gradually and measure the corresponding change in the overall elastic response.

2.1 Introduction

In Chapter 1, we gave an overview of the experimental work investigating the effects of the specimen size, relative to the cell size, on the measured mechanical properties of cellular solids (see Section 1.3). Experiments indicate that when the specimen size (and/or the loading wavelength) and the cell size are of the same order of magnitude, the individual response of cells varies considerably throughout the specimen. This leads to differences in the macroscopic response from one specimen to another with a different size. Classical continuum theory does not incorporate a length scale, and therefore cannot capture size-dependent behaviour. One approach to account for size effects, which will be followed in this chapter, is to explicitly account for the cellular morphology by modelling individual cell walls (or cell faces) by using the finite element method (see e.g. Andrews *et al*. [2001], Onck *et al*. [2001], Chen and Fleck [2002], Diebels and Steeb [2002]).

Our aim in this chapter is to investigate the size effects (and their physical grounds) in the mechanical behaviour of foams. To mimic the behaviour of real foams, we use two-dimensional microstructures (honeycombs), with both regular (square, hexagons) and irregular (perturbed hexagons, Voronoi tessellations) microstructures. In section 2.2, we introduce the mechanical properties and the deformation mechanisms of some two-dimensional microstructures, including the ones used in here. We discuss the effect of imperfections (such as cell wall misalignments, cell wall waviness, cell size variations, etc) on the mechanical behaviour of cellular solids, and modify our models accordingly to be able to represent metal foams more realistically. In section 2.3, we perform simple shear, uniaxial compression and pure bending tests on specimens with different microstructures. We change the specimen size gradually to detect the size effects. Finally, section 2.4 summarizes the size effects observed for each boundary value problem and comments on the underlying mechanisms.

2.2 Two-dimensional cellular solids

In this section, we discuss the mechanical behaviour of regular and irregular two-dimensional cellular solids and analyze their usefulness in representing real three-dimensional foam structures.

2.2.1. Regular cellular solids

Regular two-dimensional cellular solids (also referred to as lattices or honeycombs) are often used as two-dimensional representations of more complex three-dimensional

foams. They enable closed-form expressions for the macroscopic in-plane properties as a function of the cell wall thickness t and length l, and the properties of the cell wall material (subscript s), the Young's modulus E_s, the Poisson's ratio ν_s, and the yield stress σ_{ys}. The three simplest lattice structures are the hexagonal structure, the square structure and the fully triangulated structure (see Fig. 2.1). Due to six-fold (hexagonal) symmetry (i.e. a structure has the same appearance six times in a 360° rotation around its centre), the triangulated and hexagonal structures are isotropic in

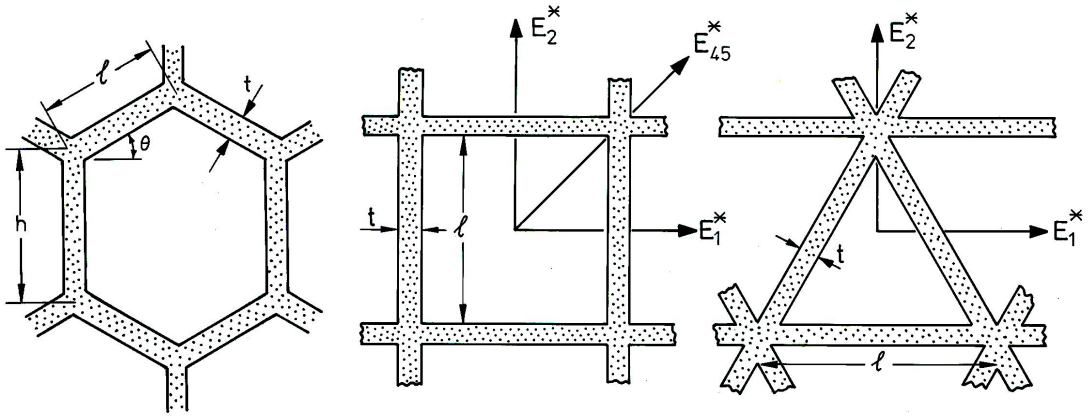

(a) (b) (c)

Figure 2.1: Regular two-dimensional cellular solids. (a) Regular hexagonal structure. (b) Square structure. (c) Triangular structure. (Reproduced, with permission, from Gibson and Ashby [1997]).

the plane (see e.g. Wang and Stronge [1999], Warren and Byskov [2002]), while the square structure, with four-fold symmetry, is orthotropic (see e.g. Ostoja-Starzewski *et al*. [1996]). For the low density isotropic structures, the Young's modulus can be written as

$$\frac{E^*}{E_s} = \frac{4}{\sqrt{3}} \left(\frac{t}{l} \right)^3 \tag{2.1}$$

for the hexagons[1] (Gibson *et al*. [1982]), and

$$\frac{E^*}{E_s} = \frac{2}{\sqrt{3}} \frac{t}{l} \tag{2.2}$$

for the triangles (Christensen [1995]). The square structure has two stiff directions, parallel to the cell walls,

[1] Neglecting shear deformations.

$$\frac{E_1^*}{E_s} = \frac{E_2^*}{E_s} = \frac{t}{l}, \tag{2.3}$$

and two compliant directions at 45^o (Gibson and Ashby [1997]),

$$\frac{E_{45}^*}{E_s} = 2\left(\frac{t}{l}\right)^3. \tag{2.4}$$

The difference in stiffness between these structures is clearly exemplified by plotting Young's modulus as a function of the loading direction with respect to the microstructural orientation (see Fig. 2.2). The triangular and hexagonal structures are isotropic with the former being much stiffer than the latter. The underlying reason for this behaviour is the difference in the deformation mechanisms for different cell

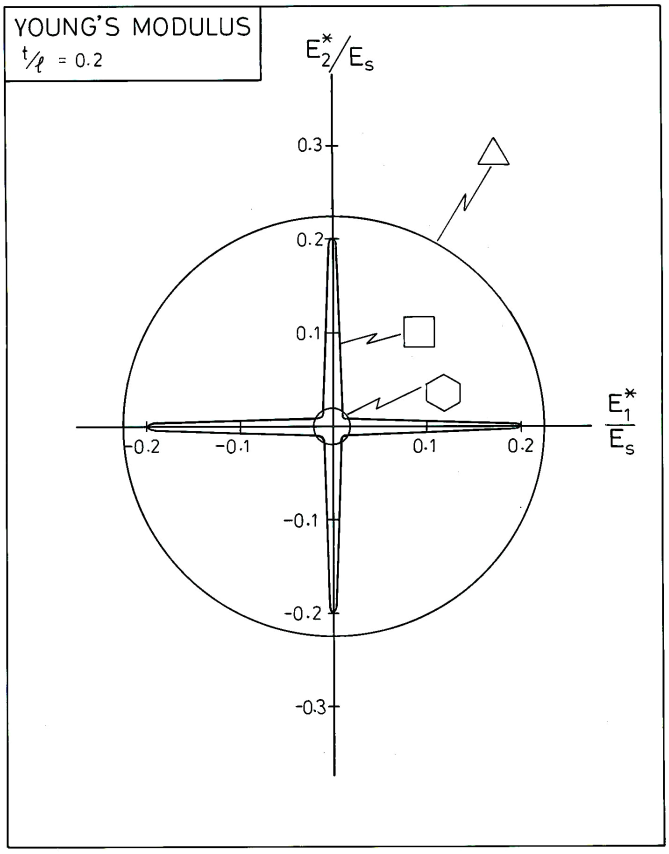

Figure 2.2: Young's modulus as a function of loading direction for triangular, square and hexagonal cells. The square structure is orthotropic with a low stiffness at 45^o and a high stiffness at 0^o and 90^o. The hexagonal and triangular structures are isotropic, having a low and high stiffness, respectively. (Reproduced, with permission, from Gibson and Ashby [1997]).

topologies: cell wall bending versus cell wall stretching (see Grenestedt [1999], Deshpande *et al*. [2001a, b]). The hexagons and squares-at-45^o (i.e. loaded in the diagonal direction) deform by cell wall bending, leading to a cubic dependence on *t/l* (see Eqs. 2.1 and 2.4), while the triangular structure and the square structure loaded parallel to the cell walls deform by cell wall stretching, leading to a linear dependence on *t/l* (see Eqs. 2.2 and 2.3). The uniaxial plastic properties of these structures show a comparable dependence on *t/l* (quadratic when bending-dominated and linear when stretching-dominated). Note that Fig. 2.2 is plotted for the same *t/l* value for all three microstructures, which means that the relative density is slightly different for each case.

A similar difference in bending versus stretching response is observed for three-dimensional models of perfect (i.e. without imperfections) cellular solids (Gibson and Ashby [1997]). A more suitable scaling quantity of the mechanical properties of three-dimensional foams is the relative density ρ. The relative density is the density of the cellular material divided by the density of the cell wall material, and it scales with $(t/l)^2$ for open-cell foams and with t/l (here t is the thickness of the cell faces) for closed-cell foams. Open-cell foams deform by bending, yielding a quadratic dependence on ρ for stiffness and a power 3/2 dependence for plastic strength. Closed-cell foams, on the other hand, deform by stretching of the cell faces, giving a linear dependence on ρ for both stiffness and strength. Table 2.1 summarizes these scaling relations for cellular solids having a perfect cellular structure.

Table 2.1

Scaling relations for perfect cellular solids.

	Relative density	Stiffness	Plastic strength
2D cellular solids	$\rho \propto t/l$		
1. bending-dominated		$E^*/E_s \propto \rho^3$	$\sigma^*_{pl}/\sigma_{ys} \propto \rho^2$
2. stretching-dominated		$E^*/E_s \propto \rho$	$\sigma^*_{pl}/\sigma_{ys} \propto \rho$
3D open-cell foams	$\rho \propto (t/l)^2$	$E^*/E_s \propto \rho^2$	$\sigma^*_{pl}/\sigma_{ys} \propto \rho^{3/2}$
3D closed-cell foams[¶]	$\rho \propto t/l$	$E^*/E_s \propto \rho$	$\sigma^*_{pl}/\sigma_{ys} \propto \rho$

[¶]Assuming all material is in the cell faces (having a thickness t).

Experiments on closed-cell metal foams, however, show a scaling that closely resembles that of open-cell foams, owing to the fact that imperfections in the cell faces (such as curvatures, corrugations and cracks) reduce their mechanical contribution, promoting bending of the cell edges to be the dominant deformation mechanism (Sugimura *et al*. [1997], Simone and Gibson [1998b], Bart-Smith *et al*. [1998], Andrews *et al*. [1999]). Analytical and finite element models of closed cell

foams accounting for such imperfections are in good agreement with these experiments (Simone and Gibson [1998a], Grenestedt [1998]). Due to the random distribution of cell size and shape, the overall mechanical properties of three-dimensional foams are isotropic. Since the two-dimensional hexagonal structure is isotropic and deforms by cell wall bending as well, it is an attractive model material for the elastic and plastic behaviour of real three-dimensional foams in case of uniaxial loading.

2.2.2 Irregular cellular solids

Although hexagons are useful as a model material under uniaxial stress states, under multiaxial stress states, however, the mechanical behaviour of regular hexagons diverges from that of real metal foams. When hexagons are loaded equi-biaxially (macroscopic normal stresses $\sigma_1=\sigma_2$), all internal bending moments in the structure vanish, causing cell wall stretching to be the dominant deformation mechanism. As a result, the yield strength under hydrostatic loading (i.e. in-plane equi-biaxial compression) is much higher than under deviatoric loading (such as uniaxial compression), making the yield surface elongated in the $\sigma_1=\sigma_2$ direction, see Fig. 2.3.

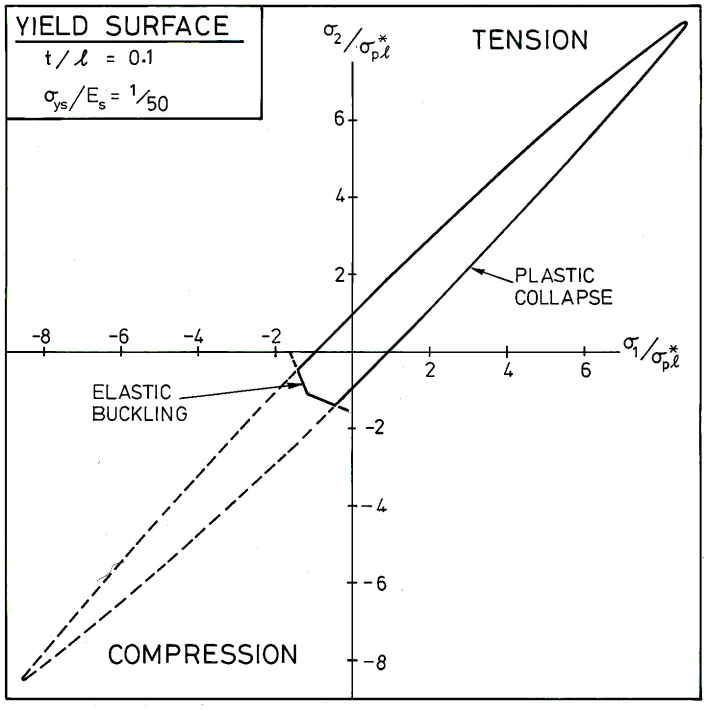

Figure 2.3: The yield surface for a regular hexagonal structure for t/l=0.1. Stresses are normalized with the uniaxial plastic strength $\sigma^*_{pl}=2/3\ (t/l)^2$. (Reproduced, with permission, from Gibson and Ashby [1997]).

A similar conclusion can be drawn for the elastic properties in terms of the bulk modulus versus Young's modulus. Experimentally-obtained yield surfaces of real foams, however, are approximately circular in the deviatoric-hydrostatic stress space (e.g. Gioux *et al*. [2000], Deshpande and Fleck [2000], Doyoyo and Wierzbicki [2003]), demonstrating that the yield strength under hydrostatic loading is approximately the same as under uniaxial loading. This can be traced to the fact that under both stress-states, plastic bending is the dominant deformation mode, due to the presence of imperfections. In two-dimensional structures this behaviour can be mimicked by introducing imperfections such as wiggles, missing cell-walls and cell-wall misalignments in the regular hexagonal structure, or by using Voronoi tessellations which account for the cell size variations (Grenestedt [1997], Triantafyllidis and Schraad [1998], Chen *et al*. [1999]). This causes a much bigger knock-down in the hydrostatic properties than in the uniaxial properties, leading to a circular yield surface.

Cell wall misalignments are introduced in the regular hexagonal microstructures by displacing all triple junctions with coordinates (x_1, x_2) in a random direction θ and over a random distance b, chosen from a uniform distribution [0, αl], where α is a constant and l is the cell wall length (see Fig. 2.4a). Then the new coordinates (x_1', x_2') can be written in terms of the old ones as

$$\begin{aligned} x_1' &= x_1 + b\cos\theta, \\ x_2' &= x_2 + b\sin\theta. \end{aligned} \tag{2.5}$$

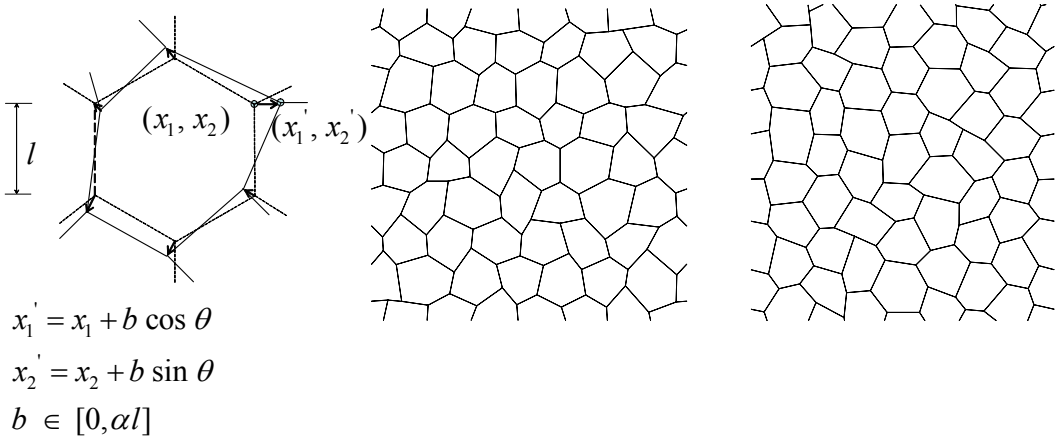

Figure 2.4: (a) Sketch illustrating the introduction of cell wall misalignments into a regular hexagonal microstructure. (b) Perturbed hexagonal microstructure in the default orientation for α=0.4. (c) Perturbed hexagonal microstructure in the rotated orientation for α=0.4.

These structures, called 'perturbed hexagons', will be adopted as one of the two-dimensional structures to study size-effects in Section 2.3. Although the perturbed hexagonal microstructures are produced in a random manner, they still might carry the underlying topological foot-print of the hexagonal "close-packed" ordering. To analyze this, two orientations of the perturbed hexagonal microstructures with respect to the loading direction will be investigated, termed the 'default orientation' (Fig. 2.4b) and the 'rotated orientation' (Fig. 2.4c), using $\alpha = 0.4$.

To account for a fully random distribution of cell sizes and shapes, we use Voronoi [1908] tessellations. The Voronoi tessellation technique is akin to a foaming process, where bubbles nucleate at random sites and expand in the liquid material. The final space-filling packing of cells is identical to a Voronoi tessellation if the following assumptions are made (see also Zhu *et al*. [2001a] and the references therein):

1. All nuclei appear simultaneously.
2. All nuclei remain fixed in location throughout the growth process.
3. For each nucleus, the growth occurs at the same rate in all directions.
4. The linear grow rate is the same for each cell associated with a nucleus
5. Growth ceases for each cell whenever and wherever it comes into contact with a neighbouring cell.

Based on these assumptions, the final shape and the size of the cells are uniquely determined by the initial distribution of the nuclei. Even though a foaming process is more complicated than the model suggested here[2], the experimentally measured topology parameters (e.g. average number of struts per cell face, average number of faces per cell, etc.) of many foams are in close agreement with those of Voronoi tessellations (see Gibson and Ashby [1997]).

To create two-dimensional Voronoi diagrams, a set of nuclei is generated in a rectangular box with area A. For a fully random tessellation (often referred to as a Γ-Voronoi), the coordinates of the nucleation points are chosen randomly (i.e. from a uniform distribution). Once all the nucleation points are created, adjacent points are connected to each other by straight lines (see the dashed lines in Fig. 2.5), resulting in a triangulation of the area, known as a Delaunay [1934] triangulation. Voronoi polygons are then generated by drawing normals that divide the dashed connector lines (i.e. the sides of the Delaunay triangles) into two and finally trimming these normals where they meet (see Fig. 2.5). We use the commercial software Matlab to create Voronoi diagrams.

[2] Typical for closed-cell metal foams is cell coalescence, as a result of which the one-to-one correspondence between nucleus and cell is lost.

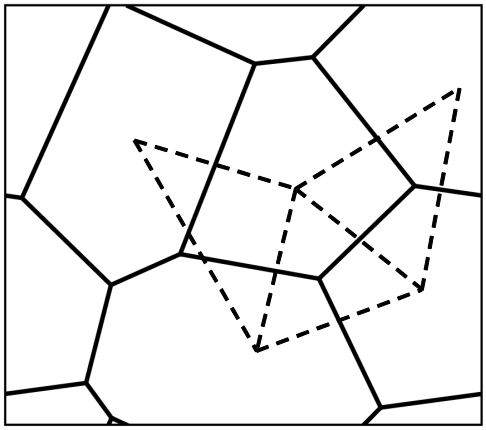

Figure 2.5: Construction of a Voronoi diagram. Adjacent nucleation points are connected to each other by straight lines (dashed). Drawing normals that divide these connector lines into two and trimming these normals where they meet generate Voronoi polygons (solid lines).

In a Γ-Voronoi the nucleation sites can be arbitrarily close together, leading to a wide distribution of cell sizes. Many open-cell foams, however, have a much narrower cell-size distribution. This can be straight-forwardly accounted for by imposing a constraint on the distribution of nuclei. One way of imposing such a constraint is to start from a distribution of nuclei corresponding to a regular hexagonal microstructure and then to displace each nucleus in a restricted area around the initial position (see e.g., Van der Burg *et al*. [1997], Fazekas *et al*. [2002]). Another method, the one employed here, is to randomly place n nucleation points in the area A such that the separation between any two nuclei must be larger than a minimum allowable distance, s (e.g. Zhu *et al*. [2000, 2001a, b]). The resulting structure is called a δ-Voronoi, to be distinguished from the fully random Γ-Voronoi. To classify the randomness, the separation distance can be normalized by a reference length r, defined as

$$r = \sqrt{\frac{2A}{\sqrt{3}n}}, \tag{2.6}$$

being the distance between any two adjacent nuclei if the n nucleation points (i.e. number of cells) in the area A, would have been distributed in a closed-packed manner so as to generate a regular hexagonal packing. The measure of randomness, $\delta = s/r$ ranges from $\delta = 1$, the regular case of perfect hexagons, to $\delta = 0$, the fully random case of a Γ-Voronoi.

Depending on the boundary value problem analyzed, we used either periodic or displacement boundary conditions in the following. The periodicity of the Voronoi diagrams is achieved by dividing the two-dimensional plane into nine equal rectangles, the one in the middle being an RVE (Representative Volume Elements)

with area A. For each nucleation point created in A, a corresponding point is created in each of the eight surrounding areas. Each subsequent nucleation point is accepted only if it is located at a distance greater than δ from the points already present. Once all nucleation points are created, the Voronoi tessellation is generated, which accounts for full periodicity of the middle area A. Finally, the periodic RVE is obtained by cutting the middle area A from the centre of the nine rectangles. Figure 2.6 shows three Voronoi structures with different levels of randomness, $\delta = 0$, 0.4 and 0.7, with periodicity being accounted for.

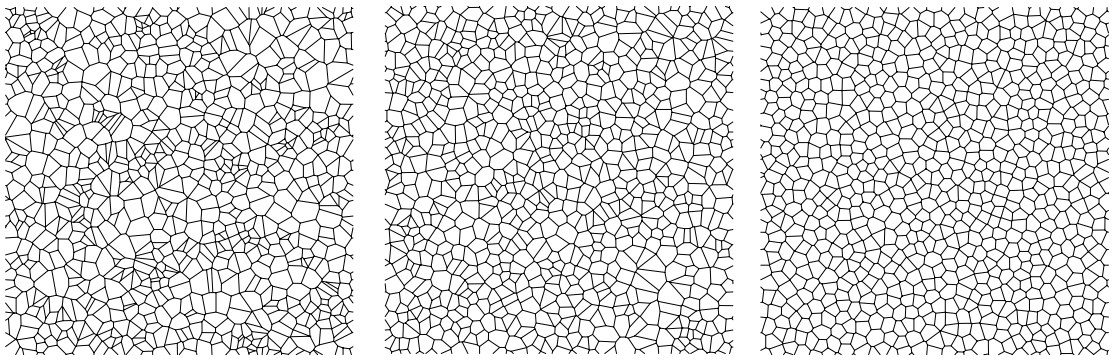

(a) (b) (c)

Figure 2.6: Voronoi tessellations: (a) δ=0. (b) δ=0.4. (c) δ=0.7. Periodicity is accounted for.

2.2.3 The effect of imperfections in Voronoi structures

As stated in the previous section, Voronoi tessellations have a less elongated yield surface than regular hexagons, due to their non-uniform cell size distribution. However, to represent real foams, a further knockdown of the hydrostatic yield strength, relative to the uniaxial strength, is needed. For this purpose, we introduced two types of imperfections in the Voronoi structures. The first one consists of cell wall misalignment as also applied on the hexagonal structures, see Fig. 2.4. In the case of the Voronoi tessellations, the lengths of the cell walls that meet at a junction are not the same. To avoid convex shaped cells, we pick the random displacement of a junction node from a uniform distribution in the range 0 to αl_{m}, where l_{m} is the minimum of the cell wall lengths among those connected to this junction. The second imperfection is cell wall waviness. To introduce cell wall waviness, we impose a lateral displacement on cell walls, in such a way that it turns a straight cell wall into a sinusoidal-shaped cell wall, according to

$$y(x) = q \sin\left(\frac{\pi x}{l}\right), \tag{2.7}$$

where q is a random number chosen from a uniform distribution $[0, \beta l]$, with β a constant, which defines the amplitude of the cell wall waviness, l is the cell wall length and x and y are the coordinates on a local Cartesian frame with x being the coordinate along the end-to-end distance. By comparing the morphology of the generated microstructures with the electron microscope images of real cellular solids, it was concluded that for α larger than 0.2 or β larger than 0.06, the microstructures are not realistic. To illustrate the morphological changes introduced by the imperfections, Fig. 2.7a shows a fully random ($\delta=0$) Voronoi diagram (i.e. $\alpha=0$, $\beta=0$, in red) on top of which the same structure is plotted having the triple points randomly displaced ($\alpha=0.2$, $\beta=0$, in green). Then, in Fig. 2.7b, cell wall wiggles are imposed on the perturbed structure (in green), resulting in a ($\alpha=0.2$, $\beta=0.06$) microstructure, in blue.

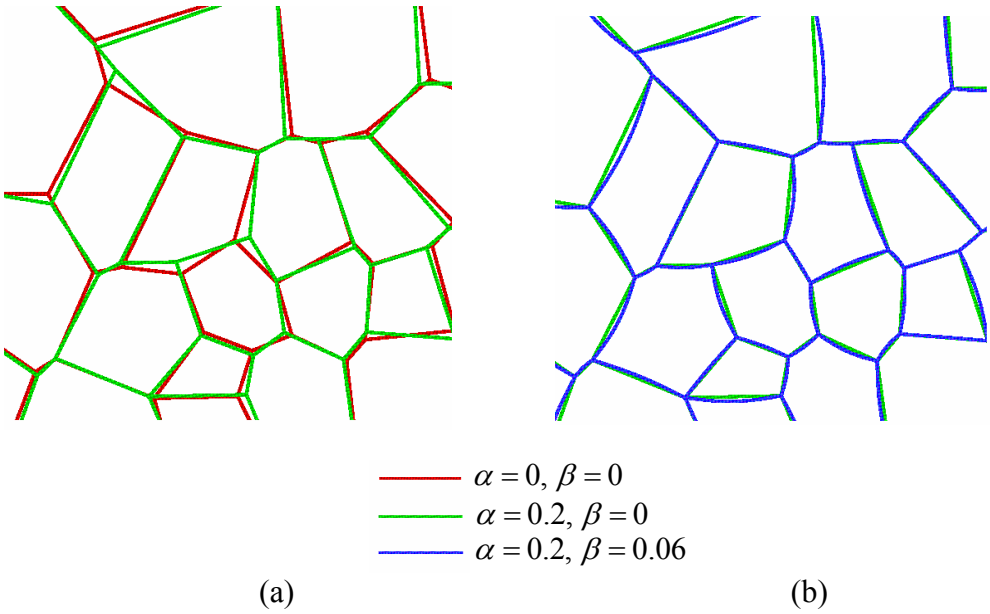

Figure 2.7: (a) Fully random ($\delta=0$) Voronoi diagram (i.e. $\alpha=0$, $\beta=0$, in red) on top of which the same structure is plotted with $\alpha=0.2$, $\beta=0$ (in green). (b) Fully random ($\delta=0$) Voronoi diagram with triple points perturbed ($\alpha=0.2$, $\beta=0$, in green) on top of which cell wall wiggles are imposed ($\alpha=0.2$, $\beta=0.06$, in blue).

To evaluate the effect of the imperfections on the yield surface of the Voronoi tessellations, we performed uniaxial compression and hydrostatic loading tests on periodic RVE's (Representative Volume Elements) with different levels of imperfections, each containing 800 cells. We assume that all the cell walls in a microstructure have the same, uniform thickness t. For two dimensional structures, the relative density ρ reduces to the area fraction of solid material; it is directly proportional to the cell wall thickness t and is given by

$$\rho = \frac{t\sum_{i=1}^{k} l_i}{L_1 L_2}, \tag{2.8}$$

where k is the total number of cell walls within the microstructure and L_1 and L_2 the side lengths of the rectangular area analyzed. To discretise the cell walls, we use quadratic Timoshenko beam elements (B22 element in ABAQUS element library). Some cell walls in random microstructures (perturbed hexagons and Voronoi tessellations) are too short to be modelled as beam elements, and their percentage increases with increasing randomness. To decrease the contribution from these stocky cell walls, we remove those with a thickness to length ratio larger than 1/2 for a relative density 0.1. One of the end nodes of any removed cell wall is deleted, and the cell walls that were connected to this deleted node are reconnected to the undeleted one. There still remain some stocky cell walls in the microstructures, with a thickness to length ratio larger than 1/3, but their percentage, even in fully random tessellations, is less than 5 percent and the error due to modelling them as beam elements is expected to be small (Chen *et al*. [1999]). To ensure that the relative density is the same for different random realizations due to the removal of stocky cell walls, we redefine the cell wall thickness after the removal process. Silva *et al*. [1995] reported that the effective stiffness of a microstructure increases with decreasing percentage of stocky cell walls, due to the decrease in the total number of degrees of freedom in the microstructure. We observe an opposite tendency, i.e., both the effective stiffness and the plastic yield strength decreases with decreasing percentage of stocky cell walls. This trend is related to the fact that after the removal of stocky cell walls the average cell wall length in the cellular materials increases (and therefore the thickness decreases to ensure a constant density), making the material more compliant.

In case of elastic deformation, only a single beam element per cell wall is sufficient for a converged solution. To investigate mesh sensitivity in case of plastic deformation, we used two different discretisation methods. The first method is to discretise each cell wall with the same number of beam elements, resulting in 16 to 20 elements per cell wall for a converged solution. The second method is to keep the length of a beam element constant and equal to the cell wall thickness t, in which case the number of beam elements used to model a cell wall is given by the ratio of the length of this cell wall, l_i, to the cell wall thickness t. This number can be 30 to 40 for relatively long cell walls, and this increases the computational time excessively. Therefore, we limited the maximum number of beam elements used to model a cell wall and change this limit to see its effect. A converged solution is obtained when the limit is set to be 10, which required much less computational time than the first method. The second method, with the maximum number of beam elements set to 10, was used for all calculations reported.

The cell wall material is assumed to be elastic-plastic with a Young's modulus of $E_s = 70$ GPa, a Poisson's ratio of $\nu_s = 0.33$, and a yield stress of $\sigma_{ys} = 130$ MPa. The relative density of the samples is chosen to be $\rho = 0.1$, which is high enough to avoid premature elastic buckling of the cell walls for the material properties used. To avoid numerical problems for the finite element calculations, we employ linear isotropic hardening using a relatively low hardening slope of $H = d\sigma/d\varepsilon = 100$ MPa. We apply periodic boundary conditions on pairs of nodes J and I, located at the same position but on the opposite edges of the boundary, by describing

$$u_p^{\mathrm{J}} - u_p^{\mathrm{I}} = \varepsilon_{pq}(x_q^{\mathrm{J}} - x_q^{\mathrm{I}}), \quad \phi_3^{\mathrm{J}} - \phi_3^{\mathrm{I}} = 0, \quad p,q=1,2. \tag{2.9}$$

The corresponding macroscopic stresses read

$$\sigma_{pq} = \frac{1}{2L^2} \sum ((x_p^{\mathrm{J}} - x_p^{\mathrm{I}})F_q^{\mathrm{J}} + (x_q^{\mathrm{J}} - x_q^{\mathrm{I}})F_p^{\mathrm{J}}), \tag{2.10}$$

where L is the length of the square Voronoi diagram, ϕ_3 is the rotation of the cell walls in the x_1-x_2 plane, $F_{\mathrm{p}}^{\mathrm{J}}$ are the reaction forces in nodes J (periodicity corresponds to $F_{\mathrm{p}}^{\mathrm{I}} = -F_{\mathrm{p}}^{\mathrm{J}}$), and the summation is carried out over all the boundary nodes J. The shear strain ε_{12} is taken to be zero. In the case of uniaxial loading, ε_{11} (ε_{22}) is incremented while letting the edges with a surface normal parallel to the x_2 (x_1) direction traction free. For the case of hydrostatic loading, ε_{11} is kept equal to ε_{22}. Similar boundary conditions were employed by Chen *et al*. [1999].

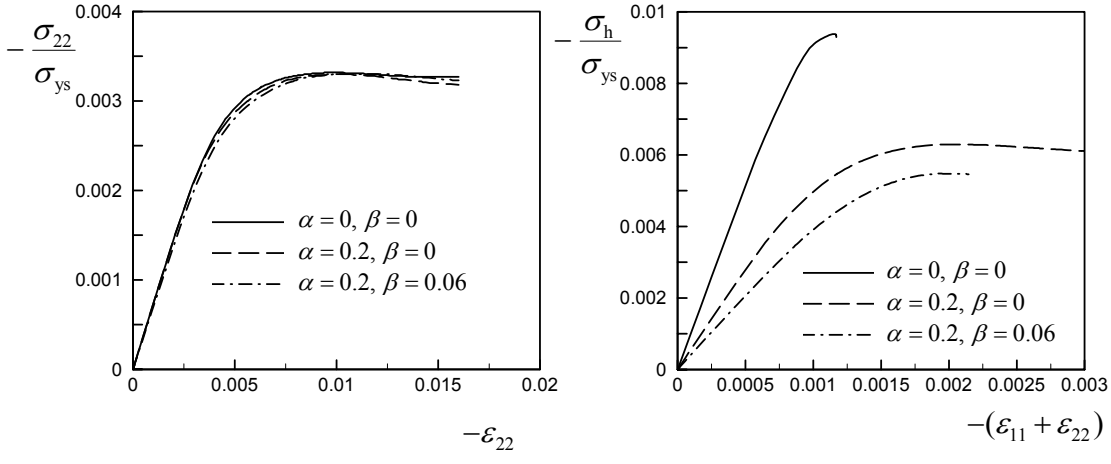

Figure 2.8: (a) The calculated compressive stress σ_{22} normalized by the yield stress σ_{ys} plotted against the compressive uniaxial strain ε_{22} for $\delta = 0$ Voronoi tessellations. (b) The calculated hydrostatic tress σ_{h} normalized by the yield stress σ_{ys} plotted against the hydrostatic strain $(\varepsilon_{11} + \varepsilon_{22})$.

Figures 2.8a and b demonstrate the results for the uniaxial and hydrostatic compressive loadings, respectively, for fully random Voronoi tessellations ($\delta = 0$). The hydrostatic stress is defined as $\sigma_h = \sigma_{pp}/2$, as in (Chen *et al*. [1999]), and the yield strength is defined by the peak of these stress strain curves. We see that either cell wall misalignments or cell wall waviness have a negligible effect on the compressive uniaxial yield strength (Fig. 2.8a). The hydrostatic yield strength, on the other hand, is highly reduced by the existence of cell wall misalignments ($\alpha = 0.2$, $\beta = 0$, Fig. 2.8b). The additional effect on the hydrostatic yield strength associated with cell wall waviness is relatively small ($\alpha = 0.2$, $\beta = 0.06$, Fig. 2.8b). Table 2.2 shows an overview of the ratio of the Young's modulus to the bulk modulus, E/κ, and the compressive yield strength to the hydrostatic yield strength, σ_u/σ_h, for Voronoi tessellations, with different δ, α and β values. It can be observed that the ratio σ_u/σ_h is smaller for more regular structures, which is in accordance with the conclusions of Chen *et al*. [1999]. The same tendency holds for the ratio E/κ as well. Note that κ and σ_h scale linearly with the relative density, while σ_u scales quadratically and E cubically.

Table 2.2

The ratio of the Young's modulus to the bulk modulus, E/κ, and the compressive yield strength to the hydrostatic yield strength, σ_u/σ_h, for Voronoi tessellations, with different δ, α and β values.

δ	0	0	0	0.4	0.4	0.4	0.7	0.7	0.7
α	0	0.2	0.2	0	0.2	0.2	0	0.2	0.2
β	0	0	0.06	0	0	0.06	0	0	0.06
E/κ	0.071	0.128	0.174	0.064	0.120	0.156	0.058	0.128	0.152
σ_u/σ_h	0.35	0.53	0.60	0.30	0.49	0.50	0.19	0.43	0.44

2.3 Size effects

In this section we investigate the effect of specimen size on the elastic response of regular (square and hexagonal lattices) and irregular (perturbed hexagons and Voronoi tessellations) cellular structures. We will explore simple shear (section 2.3.1), uniaxial compression (section 2.3.2) and pure bending (section 2.3.3) boundary value problems. All the calculations are performed assuming the strains to be small.

2.3.1 Simple shear

Figures 2.9a and b show the boundary conditions for a simple shear test on a sandwich panel having a perfect hexagonal microstructure (in the default orientation) and a Voronoi microstructure as a core, respectively. Here and in the rest of this

thesis, we will focus on Voronoi tessellations with $\delta = 0.7$, $\alpha = 0.2$ and $\beta = 0$ (see section 2.2.3). For all microstructures we use one beam element per cell wall, take a relative density $\rho = 0.1$ and use a Poisson's ratio $\nu_s = 0.33$. The results shown are normalized by the Young's modulus of the cell wall material, E_s. To have a common measure for the cell size d, both for the hexagonal microstructures (regular and perturbed) and the Voronoi tessellations, we take $d \approx 1.82l$, equal to the diameter of a circle with the same area as a regular hexagonal cell with a cell wall length l. Note that for the Voronoi structures the average cell wall length l_{av} can be deduced from the area A and the number of nuclei n, through $l_{av} = r/\sqrt{3}$, with r defined in equation 2.6. For the square microstructures, $d = l$ (see Fig. 2.1c). To avoid the edge effects common to the shear problem, we take an infinitely long material in the x_1 direction. Consequently, in case of regular microstructures such as perfect hexagons and squares, it suffices to analyze only one column of cells and to apply periodic boundary conditions on both sides of the unit cell (see the indicated region in Fig. 2.9a). For irregular microstructures, on the other hand, due to the stochastic imperfections, the unit cell is enlarged to $L \approx 143d$, still featuring periodic boundary conditions (see Fig. 2.9b).

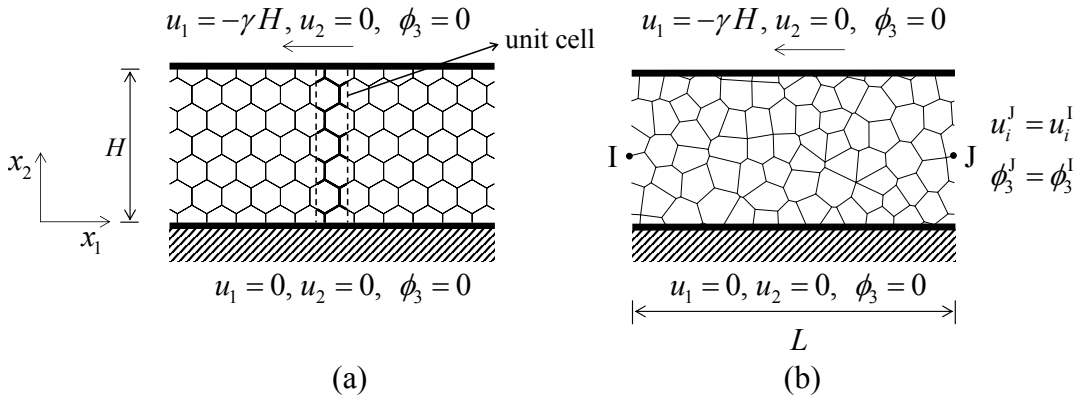

Figure 2.9: Boundary conditions for a simple shear test on a sandwich panel: (a) Perfect hexagonal microstructure in the default orientation. (b) Voronoi microstructure.

The face sheets are assumed to be rigid and perfectly bonded to the cellular material. This allows applying the boundary conditions directly to the cellular structure. At the bottom all degrees of freedom are constrained ($u_i = \phi_3 = 0$, $i = 1,2$). Note that the u_i and ϕ_3 are the displacements and rotations of the cell walls at the locations were they are connected to the face sheets. At the top a horizontal displacement is applied, $u_1 = -\gamma H$, consistent with a shear strain γ, while the other degrees of freedom are constrained, $u_2 = \phi_3 = 0$. The macroscopic shear stress is obtained by dividing the sum of the reaction forces at the top nodes by the area of the unit cell, $L\,b$, where b is the out of plane thickness and L is the length of the unit cell

in the x_1 direction. The ratio of the shear stress to the applied shear strain gives the macroscopic shear stiffness, $F/(L\gamma)$, with F the total shear force per unit out-of-plane thickness.

The value of the macroscopic shear stiffness depends not only on the relative specimen height H/d, but also on the length and the orientation of the cell walls at the boundaries, to which we refer to as the boundary configuration. To consistently check the dependence on the boundary configuration, we also analyze the regular and perturbed hexagons in a 90^o rotated orientation (termed the rotated orientation), as compared to the default orientation shown in Fig. 2.9a. For the same reason, we analyze different possibilities of "cutting specimens" for each value of H/d. As an example, Figure 2.10 shows two different cuts from a perfect hexagonal microstructure in the default orientation, with the same height, but with different boundary configurations. In the case of regular microstructures, only a limited amount of cuts (6 and 8 for the default and the rotated orientation of the regular hexagonal microstructures, respectively, and 5 for the square microstructures) are sufficient to cover almost all possible boundary configurations. For irregular microstructures

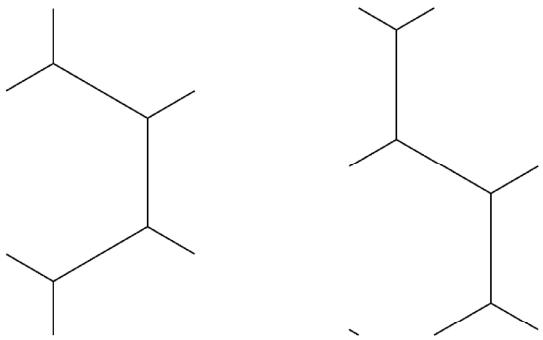

(a) (b)

Figure 2.10: Two different cuts with the same height for the regular hexagonal microstructure in the default orientation.

(perturbed hexagons and Voronoi tessellations), we take 100 different cuts. Each new sample is made by shifting the sample window (corresponding to one specific value of H/d) over a certain distance with respect to the previous sample. This distance is called the cutting step size (CSS). For the irregular calculations performed here we use CSS = $d/10$. By performing convergence tests for $H/d = 1$, 2, 3, and 5 on perturbed hexagonal microstructures, we found that for more than 100 cuts, the average and standard deviation of the macroscopic shear stiffness did not change anymore. Note that for each specimen cut, the thickness of the cell walls is adjusted to ensure that all specimens have the same relative density.

Figure 2.11 shows the macroscopic shear stiffness, $F/(L\gamma)$, normalized by the shear modulus, G, plotted against the relative specimen size, H/d, for the microstructures analyzed. Each dot in Fig. 2.11 corresponds to one finite element calculation. For each microstructure, G corresponds to the effective shear stiffness of an infinitely large block with the corresponding microstructure. For the square structure in its current orientation (see the inset of Fig. 2.11a) it is given by

$$G = \frac{1}{2} E_s (t / l)^3 \frac{1}{1 + (2.4 + 1.5\nu_s)(t / l)^2}, \tag{2.11}$$

and for the regular hexagonal microstructures, irrespective of the orientation, it is given by

$$G = \frac{1}{\sqrt{3}} E_s (t / l)^3 \frac{1}{1 + (3.30 + 1.75\nu_s)(t / l)^2}, \tag{2.12}$$

where E_s is the Young's modulus and ν_s is the Poisson's ratio of the solid material from which the cellular structure is made (see also Gibson and Ashby [1997]). For irregular microstructures, the shear modulus is found by performing a convergence test while continuously increasing the thickness of the specimens. We found that for the irregular microstructures analyzed the value of the shear modulus is approximately 10–15 percent larger compared to the regular hexagons. A comparable enhanced stiffness was found by Silva *et al*. (1995) for a δ-Voronoi structure.

For the square microstructures, we observe a large scatter in data, especially in the small H/d regime, which decreases with increasing height (see Fig. 2.11a). The overall shear stiffness increases with decreasing height, and it converges to the shear modulus with increasing H/d, given in Eq. 2.12. This stiffening behaviour, $F/(LG\gamma) > 1$, is associated with the constrained rotations of the cell walls bound to the top and bottom face sheets. It is interesting to see that weakening, i.e. $F/(LG\gamma) < 1$, is also possible for some boundary configurations for small values of H/d. This is related to the fact that we keep the density constant for all specimens, leading to thinner cell walls for some configurations. On average, nevertheless, there is a stiffening behaviour in the small H/d regime.

For the regular hexagons in the default orientation we observe weakening behaviour for some boundary configurations as well (see Fig. 2.11b), but this is absent for the hexagons in the rotated orientation (Fig. 2.11c). For the irregular microstructures (perturbed hexagons and Voronoi tessellations, Figs. 2.11d-f), the effect of the constrained boundary layers (leading to stiffening) is always dominant over the effect of the lower cell wall thickness (leading to weakening). The scatter in data for small H/d is less in case of irregular microstructures and tends to zero with

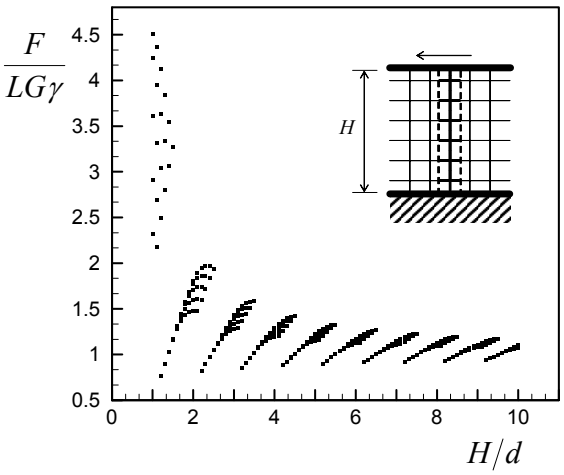

(a)

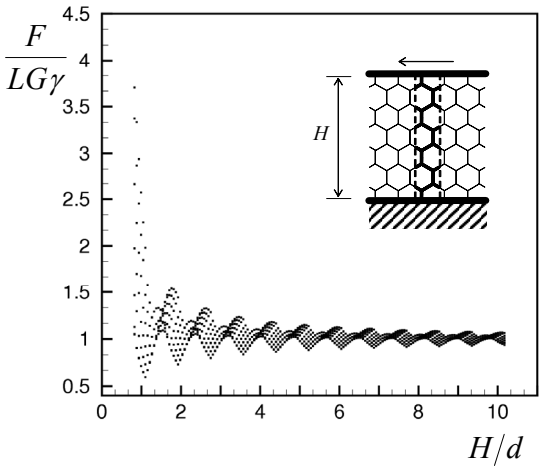

(b)

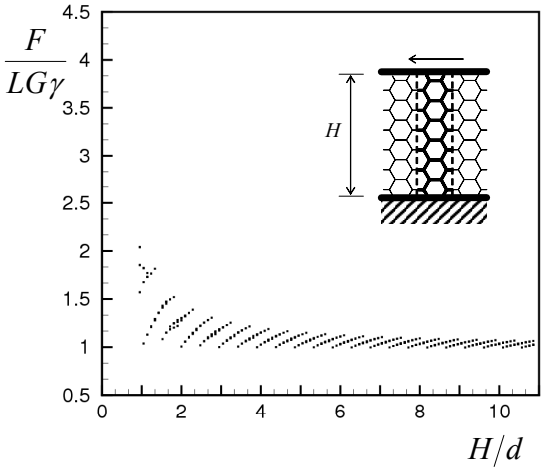

(c)

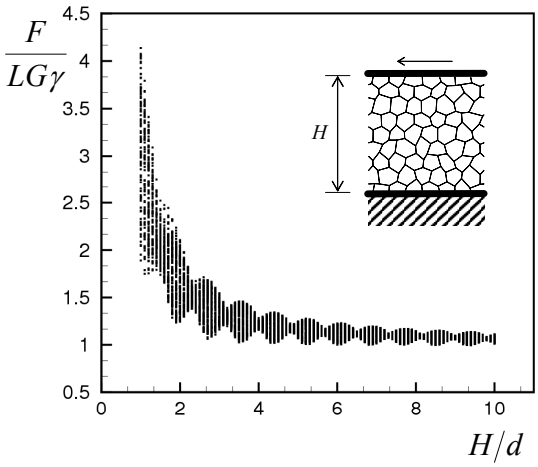

(d)

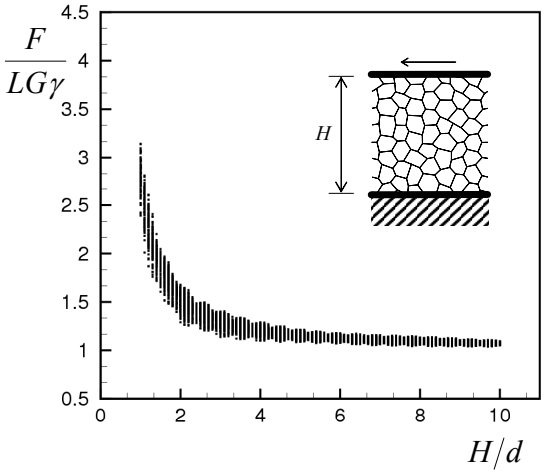

(e)

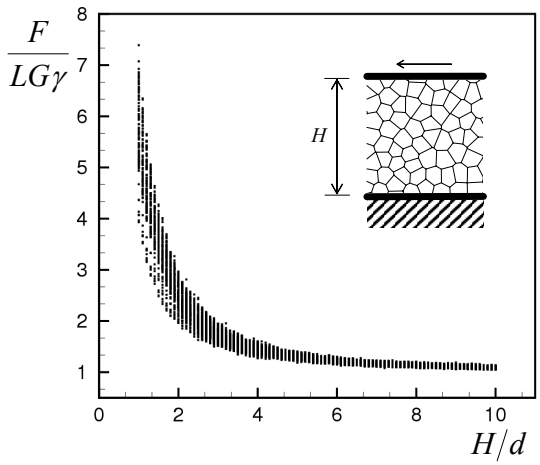

(f)

Figure 2.11: The macroscopic shear stiffness, $F/(L\gamma)$, normalized by the shear modulus, G, plotted against the relative specimen size, H/d, for the: (a) Square microstructure. (b) Perfect hexagonal microstructure in the default orientation. (c) Perfect hexagonal microstructure in the rotated orientation. (d) Perturbed hexagonal microstructure in the default orientation. (e) Perturbed hexagonal microstructure in the rotated orientation. (f) Voronoi microstructure.

increasing height. The stiffening effect is larger than it is for the regular hexagons, being largest for the Voronoi tessellations (see Fig. 2.11f).

The system parameters that determine the overall elastic response to a shear deformation are t, d, H, E_s and ν_s. From the three length scales two dimensionless quantities can be constructed: t/d (that is proportional to the relative density) and H/d. For the size effects we explored the effect of H/d for one value of the relative density. To explore the effect of t/d we repeated the calculations for values of t/d in the range 0.001–0.15. No effect was found on the $F/(GL\gamma)$ versus H/d curves, indicating that the effect of the relative density only enters through the definition of the shear stiffness G. In other words, the overall stiffness S ($=F/(L\gamma)$) can be written in terms of the system parameters (neglecting the effect of shear deformation of the cell walls) as

$$S\left(t, d, H, E_s\right) = G f\left(\frac{H}{d}\right), \tag{2.13}$$

with

$$G = cE_s\left(\frac{t}{d}\right)^3, \tag{2.14}$$

with the dimensionless constant c and the function f being specific for the cellular microstructure under consideration.

2.3.2 Uniaxial compression

We performed uniaxial compression tests for the irregular microstructures (perturbed hexagons and Voronoi tessellations) only. Figure 2.12 shows the boundary conditions for a uniaxial compression test in the x_1 direction on a perturbed hexagonal microstructure in the default orientation. We apply periodic boundary conditions on the left and the right boundaries of the structure, to imitate an infinitely long material in the x_1 direction, $u_1^{\mathrm{J}} - u_1^{\mathrm{I}} = \varepsilon_{11}(x_1^{\mathrm{J}} - x_1^{\mathrm{I}})$, $u_2^{\mathrm{J}} - u_2^{\mathrm{I}} = 0$ and $\phi_3^{\mathrm{J}} - \phi_3^{\mathrm{I}} = 0$. J and I are pairs of nodes on opposite edges of the mesh (see Fig. 2.12). The top and bottom boundary nodes are prescribed to be force and moment free. The compressive stress is calculated by dividing the sum of the reaction forces on the boundary nodes by the area under compression, Hb. The uniaxial compressive stiffness is calculated from the ratio of the compressive stress and the compressive strain, and is given by $F/(H\varepsilon_{11})$, with F being the force per unit out-of-plane thickness. The length of the specimens relative to the cell size is taken to be large enough ($L/d = 150$) to ensure that the uniaxial compressive stiffness is independent of L/d. We increase the height of the block, taking 100 different cuts for each H/d value.

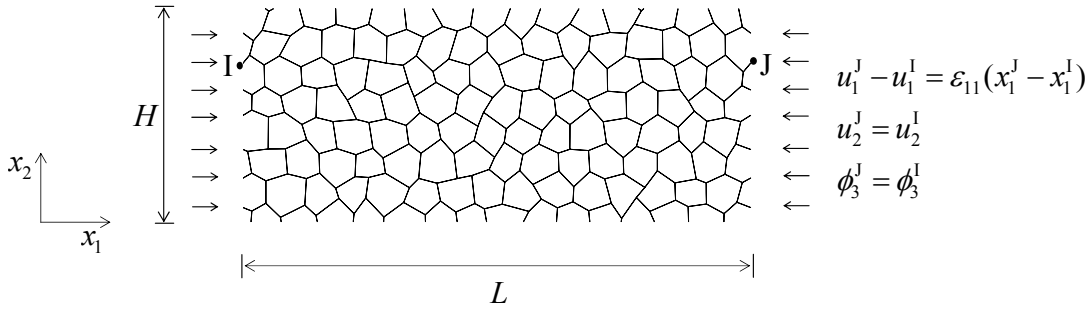

Figure 2.12: Boundary conditions for a uniaxial compression test on a perturbed hexagonal microstructure in the default orientation.

Figure 2.13 shows the calculated uniaxial stiffness, $F/(H\varepsilon_{11})$, normalized by the Young's modulus E, plotted against H/d, for different microstructures. Since the the Young's modulus of the irregular structures differs by only a few percent from that of the regular hexagonal structure we used Young's modulus of the hexagonal structure to normalize all calculations:

$$E = \frac{4}{\sqrt{3}} E_s (t/l)^3 \frac{1}{1 + (5.4 + 1.5\nu_s)(t/l)^2}, \tag{2.15}$$

see also Gibson and Ashby [1997]. We detect a severe weakening in the small H/d regime for all microstructures, with the scatter being much larger for the rotated hexagonal microstructures (Fig. 2.13b) compared to the hexagons in the default

orientation (Fig. 2.13c) and the Voronoi structures (Fig. 2.13a). Due to the boundary conditions, the cell walls located at the boundaries with a normal perpendicular to the direction of compression are stress free. In addition, the cells next to these stress free boundary layers are also less constrained than those away form the boundaries. The area fraction of this weak boundary layer, consisting of both the stress free cell walls

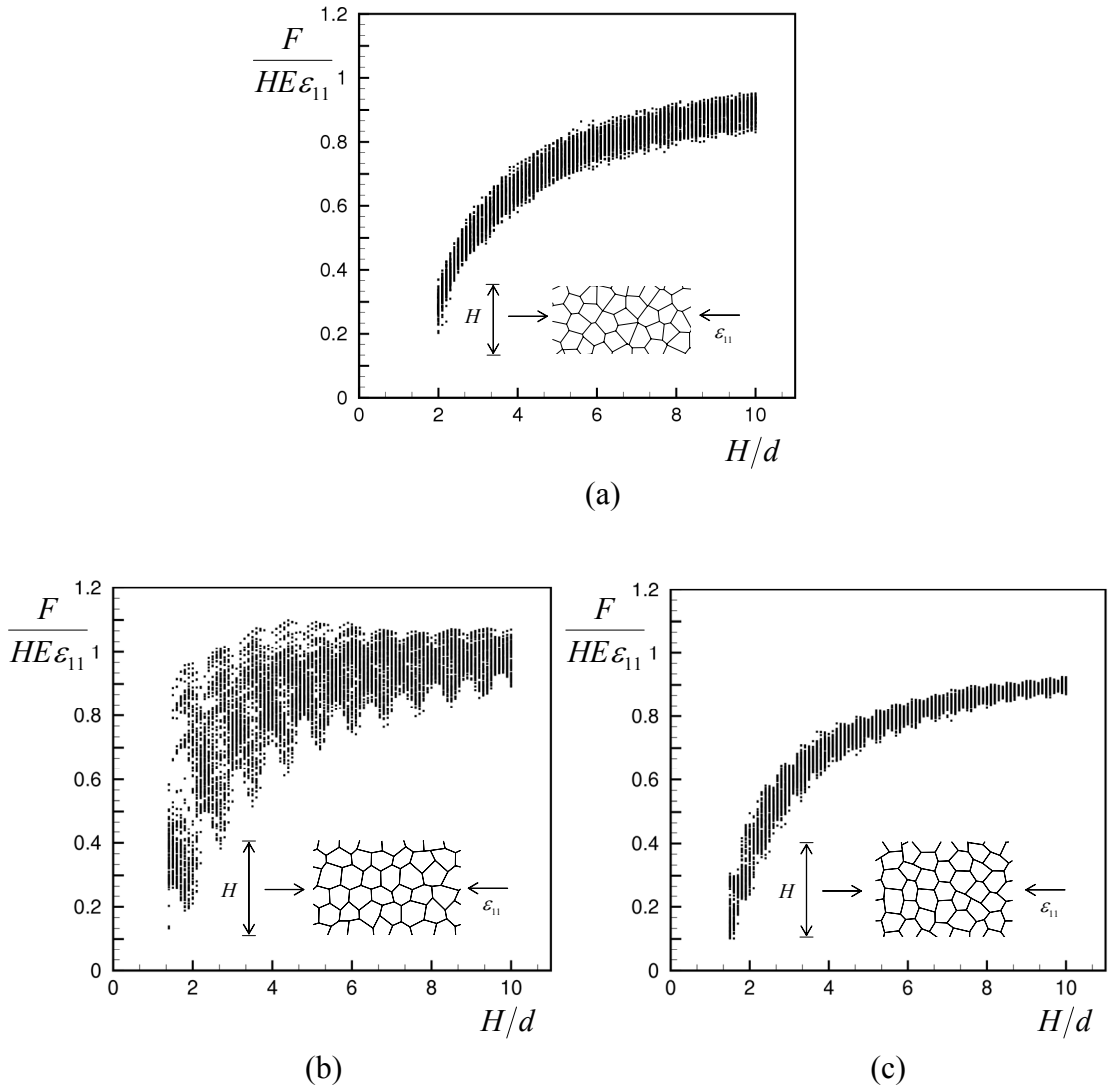

Figure 2.13: The calculated uniaxial compressive stiffness, $F/(H\varepsilon_{11})$, normalized by the Young's modulus E, plotted against H/d, for the: (a) Voronoi microstructure. (b) Perturbed hexagonal microstructure in the default orientation. (c) Perturbed hexagonal microstructure in the rotated orientation.

and the less-constrained cells, is large when the height of the specimen is small, resulting in a decrease in the macroscopic stiffness. While the specimen size increases, the contribution of this weak boundary layer to the macroscopic stiffness

diminishes and the compressive stiffness converges to the classical (bulk) value. The number of load carrying cell wall members differs from one cut to another for the same height, which is the reason for the scatter in data. The largest possible distance between two subsequent load carrying cell edges is larger for the default orientation, and therefore the scatter in data is larger as well. In the case of Voronoi microstructures, we see that the scatter is relatively low, but it shows a tendency to slightly increase with increasing *H/d*, which is the opposite of what would be expected. The reason for this is explored below.

As mentioned before, taking a long structure ($L \approx 143d$) ensures that we have enough cells in the samples so that they represent the average characteristics of the microstructure analyzed, even for small *H/d* values. On the other hand, when the samples have a large aspect ratio, there is a small additional contribution of macroscopic bending to the overall compliance. Therefore, we also analyzed the effect of the aspect ratio on the stiffness. On one side we constrain the horizontal displacements, $u_1(x_1 = 0) = 0$ (and the vertical displacements of one node to avoid rigid body translations), while we apply a horizontal displacement on the other side, $u_1(x_1 = L) = -\varepsilon_{11} L$. Calculation of the overall stresses proceeds in a similar fashion as before. Figure 2.14a shows the calculated uniaxial stiffness, $F/(H\varepsilon_{11})$, normalized by the Young's modulus *E*, plotted against the aspect ratio *L*/*H*, for Voronoi microstructures with $H/d = 3$. The solid line in Figure 2.14a passes through the average value for each aspect ratio. We see that the scatter in data is very large for small aspect ratios, whereas it converges for aspect ratios larger than 10. The sensitivity of the average value to the aspect ratio is much smaller; for aspect ratios of 1 and 5 the difference is about 10 percent, and for 2 and 5 it is about 5.5 percent. For aspect ratios larger than 5 the average value is almost the same. The average stiffness is always smaller than the corresponding bulk value (weakening behaviour) irrespective of the aspect ratio of the samples. The increase of the scatter in data for large thicknesses in case of Voronoi tessellations (see Fig. 2.13a) is associated with the fact that the length $L \approx 143d$ is kept constant while changing the thickness *H*, resulting in a decreasing aspect ratio with increasing thickness. Figure 2.14a clearly shows that a decreasing aspect ratio leads to an increasing scatter. Figures 2.14b, c and d show the calculated uniaxial stiffness, $F/(H\varepsilon_{11})$, normalized by the Young's modulus *E*, plotted against *H*/*d*, for structures with a fixed aspect ratio $L/H = 2$ for Voronoi structures, perturbed hexagons in the default and the rotated orientations, respectively. By comparing Fig. 2.13 with Figure 2.14, we see that the conclusions drawn for structures with a fixed length ($L \approx 143d$, Fig. 2.13) still holds for structures with a fixed aspect ratio $L/H = 2$ (Fig. 2.14), with the difference between the two being that for the latter case the scatter is larger and the average value is slightly shifted upwards.

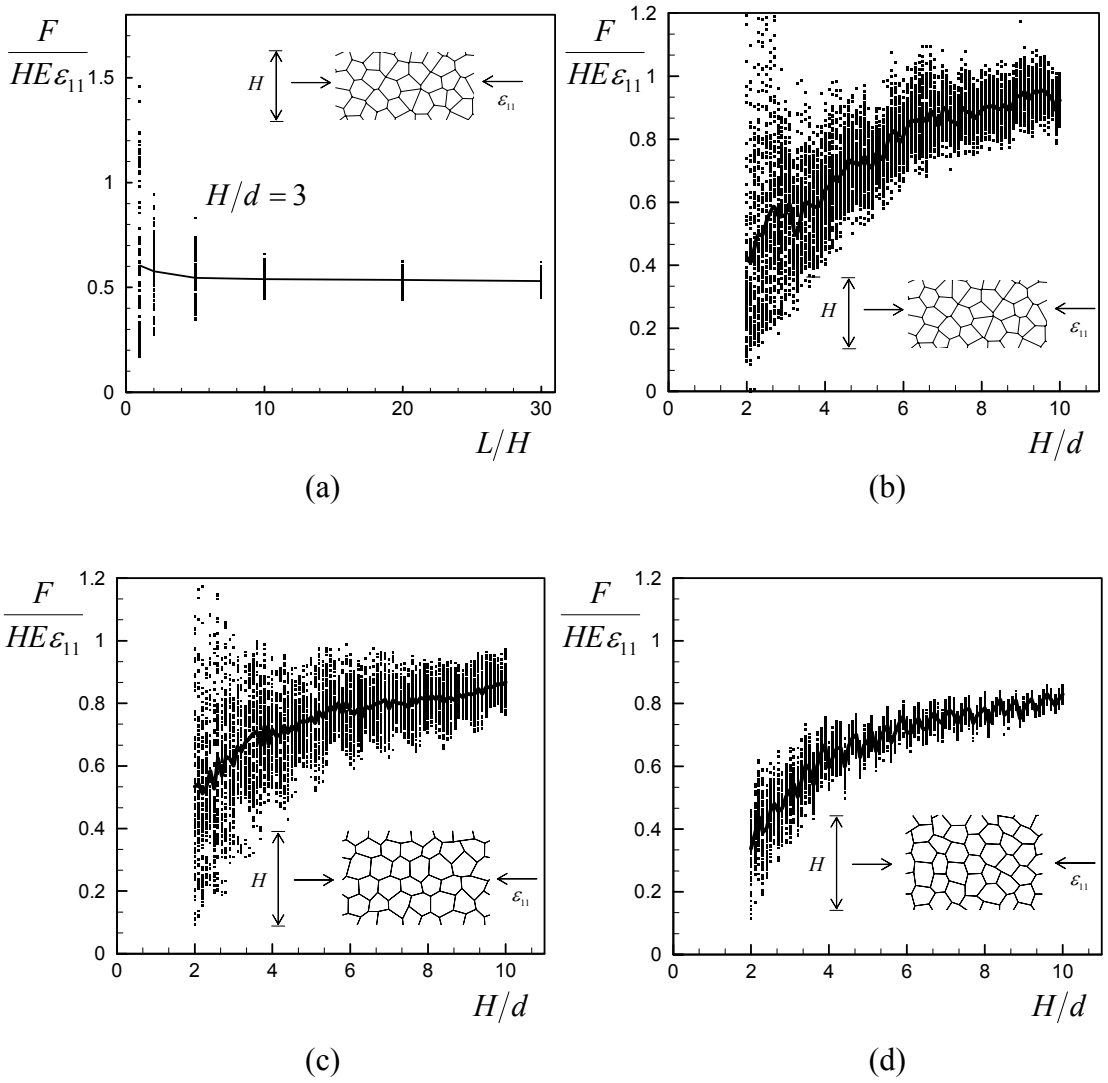

Figure 2.14: (a) The calculated uniaxial compressive stiffness, $F/(H\varepsilon_{11})$, normalized by the Young's modulus E, plotted against L/H, for the Voronoi microstructure with $H/d=3$. The calculated uniaxial compressive stiffness, $F/(H\varepsilon_{11})$, normalized by the Young's modulus E, plotted against H/d, for $L/H=2$, for the: (b) Voronoi microstructure. (c) Perturbed hexagonal microstructure in the default orientation. (d) Perturbed hexagonal microstructure in the rotated orientation.

2.3.3 Pure bending

The final boundary value problem that we solve is pure bending. The samples analyzed are similar to the one shown in Fig. 2.12. A pure bending state is achieved by fixing the left end and applying a macroscopic rotation at the right end. The

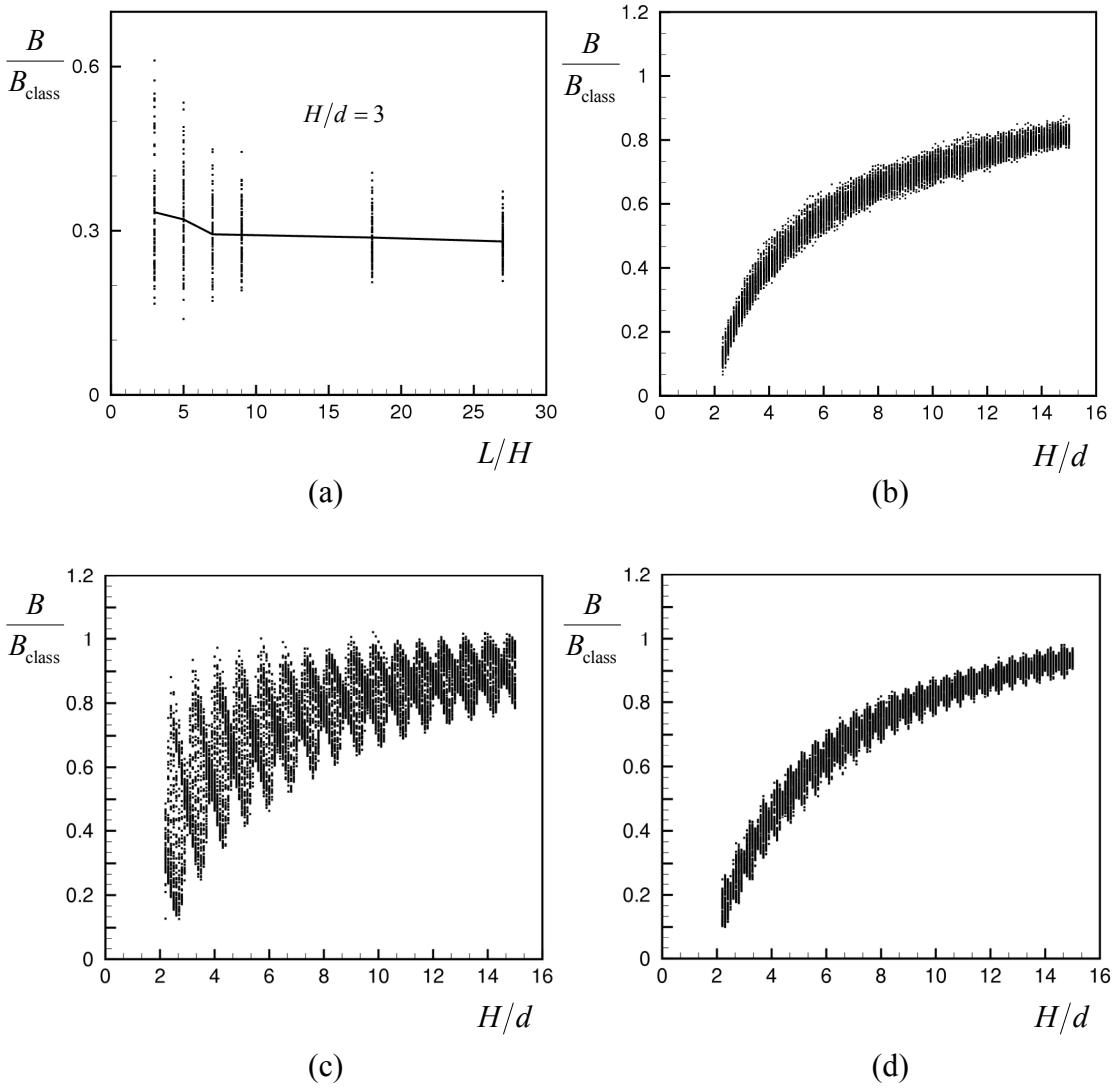

Figure 2.15: (a) The normalized macroscopic bending stiffness, B/B_{class}, plotted against L/H, for Voronoi microstructures with $H/d=3$. The normalized macroscopic bending stiffness, B/B_{class}, plotted against H/d, for the: (b) Voronoi microstructure. (c) Perturbed hexagonal microstructure in the default orientation. (d) Perturbed hexagonal microstructure in the rotated orientation.

macroscopic rotation is applied through a linearly varying displacement field over the sample height. The corresponding displacement and rotation boundary conditions at the cell walls read $u_1(x_1=0)=0$, $\phi_3(x_1=0)=0$ ($u_2=0$ for one node at $x_1=0$) and $u_1(x_1=L)=-cLx_2$. Here, x_2 is measured from the midsection of the structure and c is the curvature. The macroscopic moment is calculated from the reaction forces $f_1^{(k)}$ in the n cell walls at $x_1=L$ through

$$M = \sum_{k=1}^{n} f_1^{(k)} x_2^{(k)}. \tag{2.16}$$

The discrete bending stiffness B is calculated from M/c. The results are normalized with the classical bending stiffness of a dense sample with Young's modulus E and height H, defined as $B_{\text{class}} = EbH^3/12$ (b being the out-of-plane thickness). As in the previous section, E is taken to be the stiffness of a regular hexagonal structure, given in Equation (2.15). Figure 2.15a shows the effect of the aspect ratio on the macroscopic bending stiffness of Voronoi microstructures with $H/d = 3$. The scatter is larger for smaller aspect ratios. As it was the case for uniaxial compression, the sensitivity of the average value to the aspect ratio is very small; for aspect ratios of 3 and 7 the difference is about 12 per cent, and for aspect ratios larger than 7 the average value is almost the same. Although the sample will not be in pure bending for small aspect ratios, the results of Fig. 2.15a show that the effect of aspect ratio on the results is small. Figures 2.15b-d show the effect of specimen height on the bending stiffness for long, large-aspect-ratio samples ($L \approx 143d$) for Voronoi structures (Fig. 2.15b), and perturbed hexagonal microstructures in the default (Fig. 2.15c) and rotated orientation (Fig. 2.15d). There is a severe weakening in the small H/d regime similar to what we observed in the uniaxial compression test, and the value of the macroscopic bending rigidity converges to the classical value with increasing height. For a classical material, the material points located at the largest distance from the neutral axis would have the main contribution to the macroscopic bending stiffness. For the cellular microstructure, however, there are stress free boundaries and this causes a weakening in the bending rigidity, which is almost entirely due to the weakening in the macroscopic uniaxial stiffness. Indeed, the appearance of Fig. 2.15 is very similar to Fig. 2.13. Along these same lines, for materials which are size-independent under uniaxial loading, no size-effect is expected under bending. This is in accordance with the results for square lattices (analyzed in the Appendix) that, despite an increase in scatter, show a size-independent bending stiffness.

2.4 Conclusions

We analyzed size effects in the mechanical behaviour of cellular solids. To represent the cellular solids in two-dimensions, we used a large range of microstructures, both regular (squares and perfect hexagons) and irregular (perturbed hexagons and Voronoi tessellations). We performed simple shear, uniaxial compression and pure bending tests and analyzed the effect of the size of the samples, relative to the cell size. Figure 2.16 summarizes the effect of the specimen size on the macroscopic mechanical

properties of cellular solids. We found that in simple shear the stiffness increases with decreasing sample height, while under uniaxial compression and in bending the overall (bending) stiffness decreases with decreasing specimen width. We relate these size effects to strong boundary layers in case of shear and weak boundary layers in case of uniaxial loading and bending.

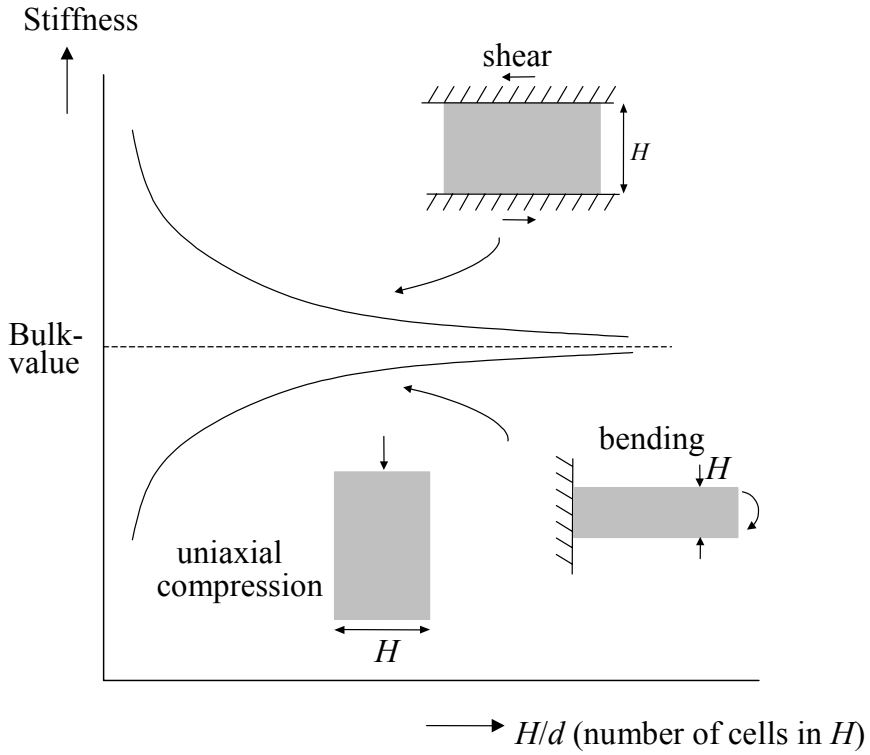

Figure 2.16: Summary of the size effects observed in the mechanical behaviour of cellular solids.

In simple shear, the cell walls connected at the top and the bottom boundaries are fully constrained, as a result of the bonding of the cellular material to the face sheets. The additional support gives rise to top and bottom regions that are stiffer than the interior regions of the material. The thickness of these strong layers depends on the boundary configuration (i.e., the length and the orientation of the cell walls at the boundaries), and we estimate them to be between 1 and 2 cell sizes. Therefore, the specimens with a small thickness, for which the area fraction of the strong boundary layers is large, have a larger macroscopic shear modulus compared to the classical (bulk) value. With the increasing specimen thickness, the area fraction of the strong boundary layers diminishes, and the macroscopic shear modulus converges to the classical value. We noted that for some boundary configurations, in case of regular microstructures, a weakening behaviour is also possible, which is related to the fact that we keep the density the same for every specimen cut. As a result some samples have a smaller cell wall thickness and weakening can occur.

In case of uniaxial compression, the cell walls at the free edge are stress free. In addition, the cells next to these cell walls have more freedom to deform and are therefore more compliant. These two phenomena, stress free cell walls and cells that are more compliant, are responsible for weak boundary layers parallel to the free edges. The contribution of these weak layers is large for small sample heights, leading to overall weakening. With increasing specimen height, the area fraction of the weak boundary layers diminishes, and the overall stiffness converges to the classical (bulk) value. Similar conclusions can be drawn for bending, leading to one weak boundary layer in tension and one in compression. The overall weakening due to the boundary layers is slightly larger in case of bending, due to the relatively large contribution of regions away from the neutral axis.

Typical for the results presented in this chapter is the presence of the scatter, which increases with decreasing specimen size. For the shear results the scatter clearly reflects the periodicity of the microstructure in case of squares and hexagons (see Fig. 2.11). By comparing the results for the hexagons in both orientations it can be observed that the average stiffening is approximately the same, but the appearance of the scatter is very different (see Figs. 2.11b and c). Due to the introduction of randomness the periodicity reduces (perturbed hexagons, Fig. 2.11d and e) and finally vanishes for fully random structures (Voronoi tessellations, Fig. 2.11f). Note that the amount of stiffening increases with randomness (Fig. 2.11). Similar conclusions with respect to the scatter can be drawn for uniaxial compression and bending: A large difference in scatter behaviour can be observed for the perturbed hexagons depending on orientation (see Figs. 2.13 and 2.15).

Appendix: Pure bending of square lattices

In this Appendix we analyze a long slender beam having a square cellular microstructure with cell size d. We do not cover the whole range of different cuts (as is done in section 2.3.3), but instead we test two extreme cases, Type A and Type B, having different lines of symmetry (see the inset of Fig. A1). The beam is in a pure bending mode having curvature c, so that the normal strain felt by the discrete members is $\varepsilon^{(k)} = -x_2{}^{(k)}c$, with $x_2{}^{(k)}$ being the distance of horizontal member (k) from the neutral axis. The effective moment follows from the normal forces $f_1{}^{(k)}$ in the horizontal members through

$$M = \sum_{k=1}^{n} f_1^{(k)} x_2^{(k)} = E_s btK \sum_{k=1}^{n} (x_2^{(k)})^2, \tag{A1}$$

so that the discrete bending stiffness for the Type A and Type B symmetries can be written as

$$B = 2E_s btd^2 \sum_{k=1}^{(n-1)/2} k^2, \tag{A2}$$

and

$$B = E_s btd^2 \sum_{k=1}^{(n-1)/2} (2k-1)^2, \tag{A3}$$

respectively. Here, n is the number of horizontal beams, related to the height of the beam, H/d, through

$$n = \begin{cases} \mathrm{mod}(\dfrac{H}{d}), & \text{for Type A} \\ \mathrm{mod}(\dfrac{H}{d}) + 1, & \text{for Type B} \end{cases} \tag{A4}$$

The discrete bending stiffness is compared to the continuum bending stiffness, B_{class}, obtained by multiplying the stiffness of an infinitely large square material, $E_s t/d$, by the moment of inertia of a dense comparison beam, $bH^3/12$. In Figure A1, the discrete bending stiffness, normalized by the continuum bending stiffness, is plotted against the normalized height. Although the results are sensitive to the symmetry-type (A or B) no clear trend can be observed. The scatter, which is partly due to the discreteness of the stiffness and partly due to the discreteness of the

moment of inertia, increases with decreasing height. It should be noted that the cell wall thickness t for all the cuts was kept constant and equal to the cell wall thickness of an infinitely large structure with the same density. The effect of this on the results shown in Figure A1 is expected to be small.

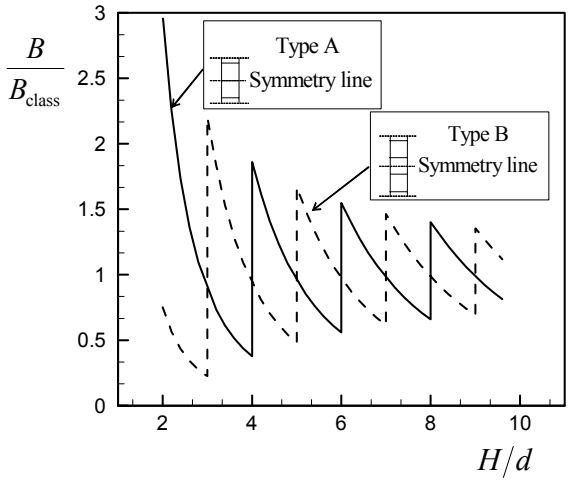

Figure A1: The normalized macroscopic bending stiffness, B/B_{class}, plotted against H/d for the square microstructure. Type A and Type B have different lines of symmetry.